Real-Time Imaging of Laser-Induced Nanowelding of Silver Nanoparticles in Solution

Ariel Rogers[1,†], Isabelle I. Niyonshuti[2,†], Alice Cai[2], Feng Wang[2], Mourad Benamara[3], Jingyi Chen[2,4,*], Yong Wang[1,4,5,*]

[1]Department of Physics, [2]Department of Chemistry and Biochemistry, [3]Institute for Nanoscience and Engineering, [4]Materials Science and Engineering Program, [5]Cell and Molecular Biology Program, University of Arkansas, Fayetteville, AR 72701.

[†]These authors contributed equally.

[*]Corresponding authors: Yong Wang (yongwang@uark.edu) and Jingyi Chen (chenj@uark.edu)

Abstract

Nanowelding of metallic nanoparticles induced by laser illumination is of particular interest because it provides convenient and controlled means for shape-conversion of nanoparticles and fabrication of nanodevices. However, the kinetics of the laser-induced nanoparticle-nanowelding remain largely unexplored. Here we exploited fluorescence microscopy to directly image the real-time nanowelding kinetics of silver nanoparticles (AgNPs) when illuminated with continuous wave laser at 405 nm. We observed that the laser illumination induced the AgNPs to form higher-order branched structures or assemblies. More importantly, we quantified the sizes of the laser-induced assemblies and found that the dependence of the average size ($\bar{A}$) of the assemblies on the illumination time t followed $\bar{A} \propto 1 - e^{-t/\tau}$. An analytical model based on simple polymerization was developed to predict and understand the measured kinetics. We experimentally verified the model by varying the laser power and the concentration of AgNPs. Furthermore, we improved the model by taking into account the merging of assemblies and predicted that the laser-induced assembling kinetics was diffusion-limited, which was then verified experimentally with AgNPs in 50% glycerol. Lastly, in contrast to the single-phased ohmic nanocontact produced by the laser-induced nanowelding, we found that the formed higher-order structures were separated into different photoluminescent domains, and that different regions of the same laser-induced assembly showed asynchronous, uncorrelated blinking behaviors. This work is expected to facilitate the development of better nanowelding strategies of metallic nanoparticles for broader applications.

Keywords: surface plasmon resonance, temperature enhancement, metal nanoparticles, nanosoldering, dynamics, model

Introduction

Metallic nanoparticles have attracted increasing attention because of their broad applications in various fields such as photonics, electronics, healthcare, energy, and environmental remediation [1–6]. In addition to their intrinsic superior optical, electronic, and chemical properties, metal nanoparticles are fundamental building blocks for developing nanodevices due to their ease of control and manipulation using various methods [7–10], including optical means [11–17]. When illuminated by light with appropriate wavelengths, localized surface plasmon resonances (LSPR) were produced in metallic nanoparticles [12,13,18,19]. Numerous applications related to LSPR in nanoparticles have been developed, ranging from sensing to imaging [18,19]. In addition, the LSPR-related photothermal effects have been extensively explored and shown to be useful [18–20]. For example, it was found that shining lasers on metallic nanoparticles could partially melt the surfaces of nanoparticles due to LSPR excitation, converting the shapes of the nanoparticles in controlled manners and/or welding them into higher-order structures or assemblies to create nanocontact or nanoconjunction [11–13,15,16,21,22]; the latter have been termed nanowelding – a process that joins/unites two or more (typically metallic) nanostructures or nanoparticles together. Such capabilities are expected to facilitate manipulation of nanomaterials and fabrication of nanodevices [3]. Therefore, it is important to develop a comprehensive understanding of the nanowelding of metallic nanoparticles.

Direct imaging of the nanowelding of metal nanoparticles is critical for obtaining a comprehensive mechanistic understanding. In the past, assemblies of metallic nanoparticles due to laser-induced nanowelding have been widely studied using *ex situ* electron microscopy, such as transmission electron microscopy (TEM), which provided snapshots before and after laser illumination [11]. Sophisticated TEM imaging was even capable of identifying the lattices formed by the laser-induced nanowelding and revealing the single-phased ohmic nanocontact [11]. However, the kinetics of nanowelding nanoparticles remain largely unexplored. In this study, we applied fluorescence microscopy to directly image the dynamic process of assembly-formation of silver nanoparticles (AgNPs) under the illumination of continuous wave (CW) laser. The wavelength of the laser used in this study was 405 nm, which is close to the LSPR peak of the AgNPs. From the movies that captured the real-time dynamics of the laser-induced assemblies due to nanowelding, we quantified the sizes of the laser-induced assemblies, and examined the kinetics (i.e., time dependence) of the average sizes of the assemblies. To understand the measured kinetics of the average sizes of the assemblies, we developed an analytical model based on simple polymerization, which fitted the observed kinetics very well. In addition, we experimentally tested the predictions from the analytical model by measuring the assembling

kinetics with different laser intensities, or with different concentrations of AgNPs, and found that the analytical model worked well. Furthermore, we developed a more general model and predicted that the laser-induced assembling is diffusion-limited, which was verified experimentally by observing the formation of assemblies in 50% glycerol. Lastly, we examined whether and how the nanowelded assemblies formed single phases in terms of photoluminescence and photophysics.

Methods and Materials

Synthesis of AgNPs.

AgNPs were synthesized via polyol reduction method [23], similar to our previous studies [24–26]. Briefly, 50 mL of ethylene glycol (EG, J.T. Baker) was added to a 250-mL 3-neck round bottom flask and heated to 150 ºC in an oil bath, followed by adding 0.6 mL of 3 mM NaHS (Alfa Aesar) in EG, 5 mL of 3 mM HCl (Alfa Aesar) in EG, 12 mL of 0.25 g polyvinylpyrrolidone (PVP, MW ~55,000, Sigma-Aldrich) in EG, and 4 mL of 282 mM CH_3COOAg (Alfa Aesar). The reaction proceeded at 150 ºC for ~1 h until the absorbance peak position of reaction mixture reached ~420 nm measured by a UV-vis spectrometer. The reaction was then quenched by placing the flask in an ice bath. Acetone was added to the mixture at a 5:1 volume ratio, and the product was collected by centrifugation. The resultant AgNPs were purified using water, collected by centrifugation, and re-suspended in water for characterization and future use.

Characterization of AgNPs.

TEM images were captured using a TEM microscope (JEOL JEM-1011) with an accelerating voltage of 100 kV. Particle size and shape were measured on the TEM images using ImageJ and an algorithmic analysis reported by Laramy et. al. [27]. High-resolution TEM (HRTEM) images were obtained on an FEI Titan 80-300 with an accelerating voltage of 300 kV. UV-vis spectra were obtained using a UV-vis spectrophotometer (Agilent Cary 50). The concentration of Ag was determined by inductively coupled plasma mass spectrometry (ICP-MS) (Thermo Scientific iCap Quadrupole mass spectrometer).

Calculation of optical spectra (LSPR) of AgNPs.

The optical spectra were calculated according to the discrete dipole approximation (DDA) using the DDSCAT 7.3 program [28,29]. In this formalism, the structure is represented by an array of dipole moments residing within its volume. Each volume element is represented as a dielectric continuum with the complex dielectric response function of bulk Ag [30]. The optical cross sections were averaged over the two orthogonal polarization directions of the incident light. The

structure of a rounded cube was built by removing 5% of the total mass from the corners of the cube. The optical efficiency, Q, is reported as the ratio of the respective optical cross section to πa_{eff}^2, where the effective radius, a_{eff}, is defined as the radius of a sphere whose volume is equal to that of the structure. Optical spectra were simulated for each structure in water.

Photoluminescence imaging of laser-induced assemblies of AgNPs.

40 µL of AgNPs in ultrapure water (>17.5 MΩ) at the desired concentration were added to a flow chamber made of coverslips and glass slides. The coverslips and slides were first cleaned with detergent, 1 M NaOH, 100% ethanol, and ultrapure water (>17.5 MΩ) sequentially [25,26], followed by plasma cleaning (Harrick Plasma, NY) [31,32]. The flow chamber was sealed using nail polish and then mounted on a fluorescence microscope for imaging [32].

The fluorescence microscope used in this study was an Olympus IX-73 inverted microscope equipped with an Olympus 100× N.A.=1.49 oil immersion TIRF objective, a multi-color laser bank (iChrome MLE, Toptica Photonics AG) and an EMCCD camera (Andor, MA). The microscope and data acquisition were controlled by Micro-Manager [33,34]. The 405 nm laser from the laser bank was used to illuminate the AgNPs for both nanowelding and imaging. The BrightLine® full-multiband 1λ P-V RWE super-resolution laser filter set (LF405/488/532/635-B-000, Semrock, Lake Forest, IL) was used. The laser-induced assemblies of AgNPs were imaged on the EMCCD camera. The effective pixel size of acquired images was 160 nm. Movies were acquired with an exposure time of 30 ms (the actual time interval between frames was 52.49 ms) and a length of 6000 frames.

Three sets of photoluminescence imaging experiments were performed. In the first set, the concentration of AgNPs was kept in phosphate-buffered saline (PBS) at 1.3 mg/mL while varying the power of the 405 nm laser, ranging from 5% to 30%. The actual laser powers at the samples were measured with a power meter (Thorlabs, NJ), ranging from ~1 mW to ~6 mW (Fig. S1). In the second set of experiments, the concentration of AgNPs ranged from 0.325 mg/mL to 1.3 mg/mL, while the power of the 405 nm laser was kept constant at 25% (~5 mW). In the third set of experiments, the solvent of the AgNPs was changed from PBS to 50% glycerol in PBS. For each set of experiments, 4 – 6 replicates were performed on different days.

Automatic identification of laser-induced assemblies of AgNPs and quantification of their sizes.

The laser-induced assemblies were identified automatically using custom Python scripts based on the scikit-image Python package [35]. Briefly, for each frame of the acquired movies, the

background was first removed using a rolling-ball algorithm [36] with a ball size of 9 pixels, followed by smoothing twice using a Gaussian filter with a standard deviation of 1 pixel. The background in the smoothed image was removed once again, followed by applying a threshold to obtain a black/white (BW) image. Edges were detected from the BW image using the Sobel filter [37], followed by dilating the edges by 3 pixels to fill possible gaps in the edges. Small objects with areas <32 pixels were removed, before performing a flood fill [38]. The filled objects were eroded with 4 pixels, followed by removing small objects (area <32 pixels). The resulting BW image was segmented into individual structures, which corresponded to the identified laser-induced assemblies. The numbers of pixels occupied by the individual structures were counted and used as the size of the assemblies of AgNPs.

Results

The AgNPs used in this study were synthesized as described previously [24–26]. The synthesized AgNPs were imaged using TEM, showing 67% cubes and 23% spheres (Fig. 1A), with an average size of 30 ± 5 nm (Fig. 1B). The extinction spectrum of the AgNPs measured by UV-vis spectroscopy displayed a peak at 420 nm (Fig. 1C, blue solid curve), which corroborated well the simulated LSPR peak of a rounded cube with an edge length of 30 nm at 430 nm (Fig. 1C, green dashed curve). The 10 nm discrepancy can be attributed to the size and shape distributions in the sample. The simulated spectra indicate that the ratio of absorption and scattering is close to 1 (Fig. 1D).

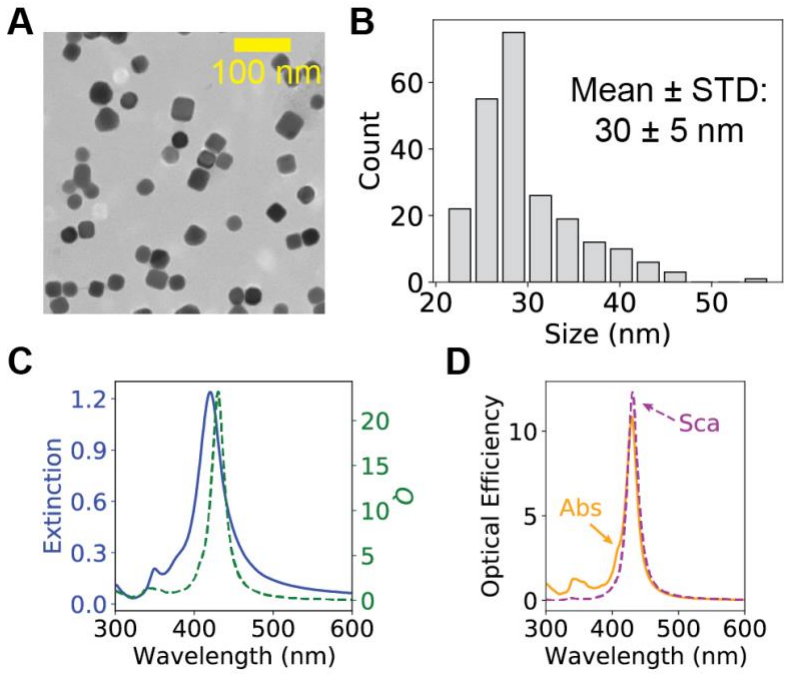

Figure 1. Characterization of AgNPs used in this study. (**A**) Representative TEM image of the AgNPs. (**B**) Size distribution of the AgNPs quantified from their TEM images. (**C**) Extinction spectrum of the AgNPs measured by UV-vis spectroscopy (blue solid curve), and DDA simulated spectrum of the extinction optical efficiency Q of a rounded 30 nm Ag cube with ~5% of the total mass removed from the corners. (**D**) DDA simulated spectra of absorption and scattering optical efficiencies of a rounded 30 nm Ag cube with ~5% of the total mass removed from the corners.

To directly image the nanowelding process of AgNPs, we shined a CW laser with a wavelength of 405 nm on the nanoparticles. The wavelength was chosen based on the LSPR peak of the AgNPs (Fig. 1D). We observed that the nm-sized AgNPs gradually formed larger assemblies and higher-order structures of μm-size, when illuminated by the 405 nm laser (Fig. 2A, and SI Movie M1). The higher-order assemblies showed higher photoluminescence than individual AgNPs, facilitating the identification of the assemblies. To quantify the nanowelding/assembling kinetics, we processed the frames of the movies using the scikit-image Python package by background subtraction, smoothing, and edge-detection (Fig. S2), identified the laser-induced assemblies (Fig. 2B), and quantified their individual sizes (i.e., the number of pixels covered by the individual assemblies). We observed that the average size ($\bar{A}$) increased with illumination time (Fig. 2C), and that the assembling kinetics could be fitted well with $\bar{A}(t) = A_0 \times \left(1 - e^{-t/\tau}\right)$ (red dashed line in Fig. 2C) where t is the illumination time and τ is the fitted characteristic time constant (154 ± 1 s).

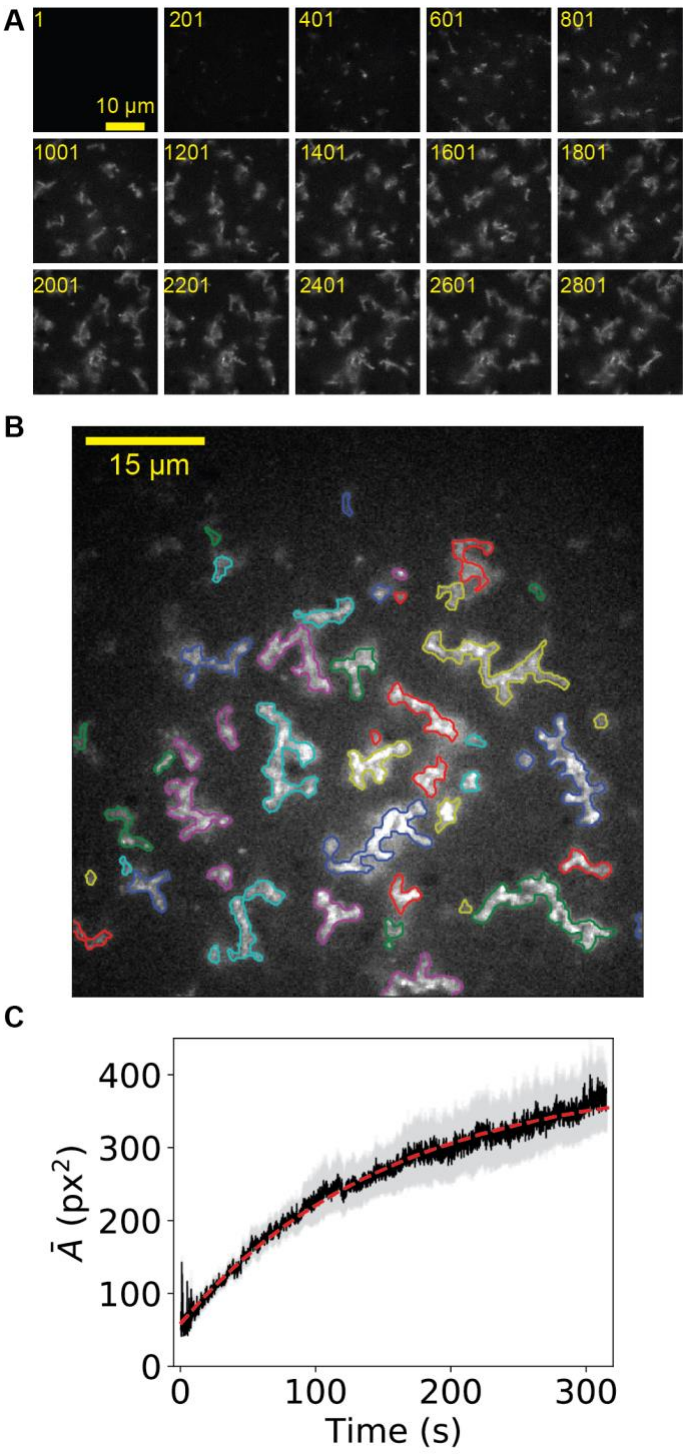

Figure 2. Direct imaging of the laser-induced nanowelding of AgNPs. (**A**) Representative photoluminescence images of laser-induced assemblies of AgNPs when illuminated by 405 nm laser at 30% power (~6 mW). Scale bar = 10 µm. Numbers indicate the frame number of the acquired movie (SI Movie M1). (**B**) Examples of the identified assemblies. Scale bar = 15 µm.

(**C**) The average size of the laser-induced assemblies as a function of time (1 px = 160 nm, or 1 px^2 = 2.56×10^4 nm^2). The black solid line is the average from five replicates, while the light gray area represents the standard error of the mean from the five replicates. The red dashed line is the fitted curve using $\bar{A}(t) = A_0 \times \left(1 - e^{-t/\tau}\right)$.

It was found that the kinetics of laser-induced nanowelding/assembling of AgNPs can be quantitatively described by a simple analytical model based on polymerization, which has been used in several scenarios including the growth of microtubules and F-actins [39]. In this simple model, an assembly with a size of n grows into a larger one (with a size of $n + 1$) with a growth rate of k by adding a monomer to the assembly (Fig. 3A). If p_n is the probability of finding an assembly of size n, we have

$$\frac{dp_n}{dt} = kp_{n-1}p_1 - kp_np_1. \tag{1}$$

For monomers, the probability p_1 satisfies

$$\frac{dp_1}{dt} = \sum_{n=1}^{\infty} - kp_1p_n = -kp_1\,, \tag{2}$$

which gives a simple exponential decay, $p_1(t) = p_1(0)e^{-kt} = p_0e^{-kt}$, where $p_0 = p_1(0)$. In this framework, the average size of the assemblies is

$$\bar{A} = \sum_{n=1}^{\infty} A\,(n)p_n = \sum_{n=1}^{\infty} n\,ap_n\,, \tag{3}$$

where a is the size of the monomers. Then its changing rate is

$$\frac{d\bar{A}}{dt} = \sum_{n=1}^{\infty} n\,a\frac{dp_n}{dt} = akp_0^2e^{-2kt}\,, \tag{4}$$

where we have plugged in Eq. (1) and (2) and carried out simplifications. Therefore, the predicted kinetics for the average size of laser-induced assemblies from this simple model is

$$\bar{A}(t) = \frac{1}{2}ap_0^2(1 - e^{-2kt}) = A_0(1 - e^{-2kt})\,, \tag{5}$$

where $A_0 = \frac{1}{2}ap_0^2$, which is consistent with the measured kinetics (Fig. 2C). Also, the model indicates that the characteristic time constant for the nanowelding/assembling kinetics is $\tau = 1/2k$. With increasing rate k (or decreasing τ), the growth of the assemblies becomes faster (Fig. 3B). Note that the parameter k in the model is variable for and dependent on the laser-induced assembling conditions, such as laser power and/or viscosity of the solution. As the probabilities (p_n) are proportional to the concentrations of the AgNPs (c_n). Thus, we thus have $A_0 \propto c_0^2$ where $c_0 = c_1(0)$ is the initial concentration of AgNPs. Therefore, we also have

$$\bar{A}(t) \propto c_0^2(1 - e^{-2kt}). \quad (6)$$

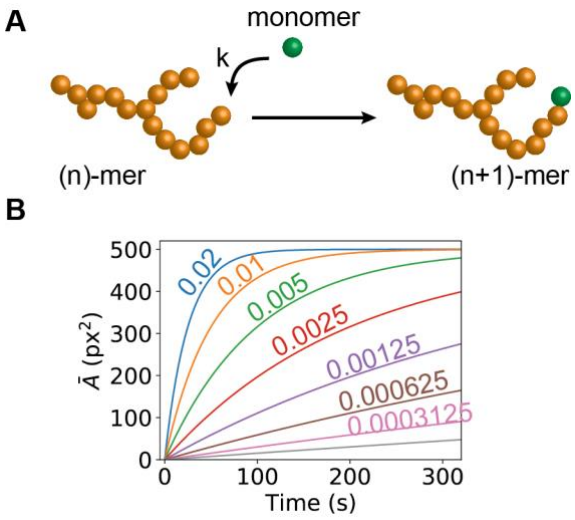

Figure 3. A simple analytical model based on polymerization. (**A**) The laser-induced assemblies grow from n-mer to (n+1)-mer by adding a "monomer" with a growth rate of k. (**B**) Model-predicted average sizes of the assemblies as functions of time with different growth rates (k). Colored numbers indicate the corresponding k values.

The analytical model predicts that, for AgNPs with a given size (i.e., fixed a) at a given initial concentration (i.e., fixed c_0), the nanowelding/assembling kinetics of AgNPs relies on the growth rate k (Fig. 3B). Because (1) the nanowelding/assembling is induced by laser illumination and (2) the LSPR and temperature enhancement of the surfaces of AgNPs is positively correlated to the laser intensity/power, we hypothesized that the growth rate k, and thus the nanowelding/assembling kinetics, would depend on the laser power. To test this hypothesis, we varied the power of the 405 nm laser from 5% (~1 mW) to 30% (~6 mW), visualized the growth of the laser-induced assemblies, and observed that increased laser power resulted in faster nanowelding and larger assemblies, although the average size increased for all the different laser powers (Fig. S3). This observation was quantitatively confirmed by quantifying the time dependence of the average sizes of the AgNP-assemblies induced by the 405 nm laser at different powers (Fig. 4A). In addition, we fitted the experimental data with Eq. (6) to extract the assembling rates (k). Note that, as the initial concentration of the AgNPs were kept constant in this set of experiments, c_0 in Eq. (6) was the same for the different curves in Fig. 4A. Therefore, we performed a global fitting (using the *lmfit* Python package [40]) with Eq. (6), in which c_0 was

kept constant but k was varied for different laser powers. From the global fitting, the growth rate k was confirmed to increase for higher laser powers (Fig. 4B). Interestingly, the dependence of the fitted rate k on the laser power P was nonlinear (Fig. 4B); instead, the k-P relation was quadratic (inset of Fig. 4B). The global fitting was overall successful; however, it is worthwhile to point out that one of the curves (at 20% laser power) was not fitted as well as the others (Fig. 4A and 4B), although all the curves could be individually fitted very well by the model (Fig. S4A). This observation implies that globally fitting of 6 curves with a model of 7 parameters is likely to impose too many restrictions and that the model may be improved by taking into account other factors, such as the merging of two smaller assemblies as investigated below.

In the analysis above, we estimated the sizes of the laser-induced assemblies or structures by the areas (i.e., the number of pixels) of the projected 2D images of the 3D structures, with the assumption that the projected 2D area is positively correlated with the number of AgNPs in (and 3D volume of) the laser-induced structures. To cross-verify the validity and robustness of the area-based analysis, we repeated the analysis but using the intensity of the structures as an alternative way for the estimation of the size of the assemblies. We observed that, although larger standard errors of the means were present in the intensity-based analysis (Fig. S4B), the intensity-vs-time curves resembled the area-vs-time curves and could be fitted by the same kinetics (i.e., Eq. (5) and (6)). More importantly, we performed global fitting on all the intensity-based curves (Fig. S4C) and found that the fitted growth rates k depended on the laser power P quadratically (Fig. S4D), consistent with the area-based analysis (Fig. 4B). Therefore, we concluded that estimating the size of the laser-induced structures from the projected 2D area is valid and justified. In addition, as the area-based analysis showed lower errors than the intensity-based analysis, we adopted the former for the quantitative analysis below.

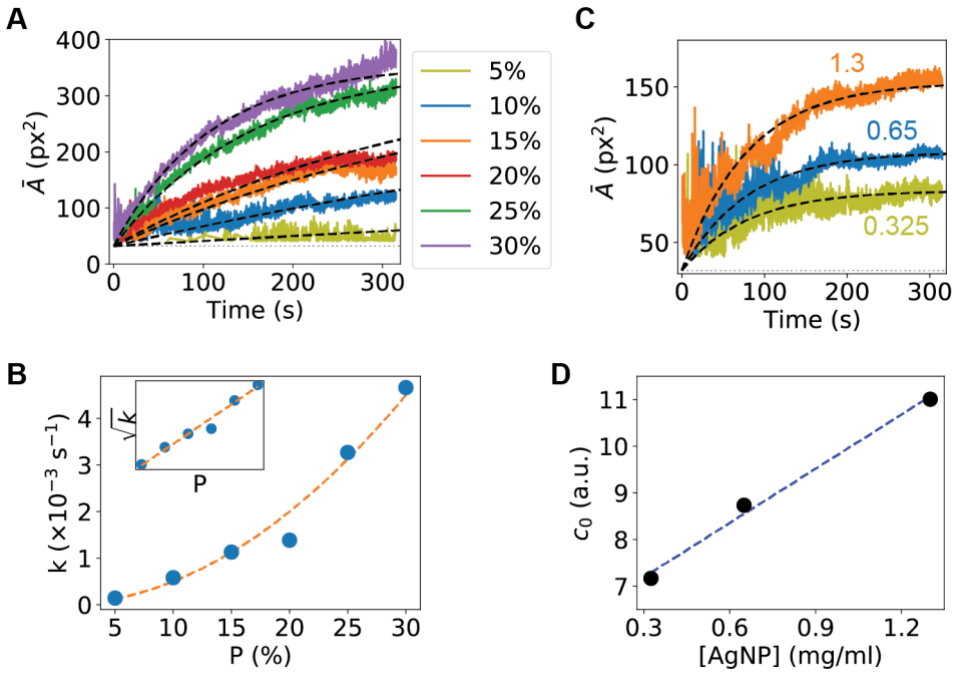

Figure 4. Dependences of the laser-induced nanowelding kinetics of AgNPs on the laser power and the initial concentration of AgNPs. (**A**) The average sizes of the laser-induced assemblies of AgNPs as functions of time when illuminated with a 405 nm laser at different power levels, ranging from 5% (~1 mW) to 30% (~6 mW). The colored solid lines represent the average from 4–6 replicates. The black dashed lines are globally fitted curves using Eq. (6). (**B**) Dependence of the fitted growth rate k on the laser power P. The orange dashed line is a quadratic fitting. Inset: $\sqrt{k}$-P relation for the same data. (**C**) The average sizes of the laser-induced assemblies of AgNPs as functions of time with varying initial concentrations of AgNPs, ranging from 0.325 mg/mL to 1.3 mg/mL. The colored solid lines represent the average from 4–6 replicates. The black dashed lines are globally fitted curves using Eq. (6). (**D**) Dependence of the fitted c_0 on the actual initial concentration of AgNPs. The blue dashed line is a linear fitting. In panels A and C, 1 px = 160 nm, or 1 px^2 = 2.56×10^4 nm^2.

The analytical model also predicts that the kinetics of the laser-induced assemblies rely on the initial concentration of the AgNPs (c_0) for a given laser power. To verify this prediction experimentally, we varied the initial concentration of the AgNPs from 0.325 mg/mL to 1.3 mg/mL while keeping the laser power constant at 25% (~5 mW). We observed that the average size of the laser-induced assemblies grew faster as the concentration of AgNPs increased (Fig. 4C and Fig. S5), consistent with the prediction from the analytical model. A global fitting of the data (same k but different c_0 for different curves in Fig. 4C) showed that the fitted c_0 was linear to the actual concentration of the AgNPs (Fig. 4D).

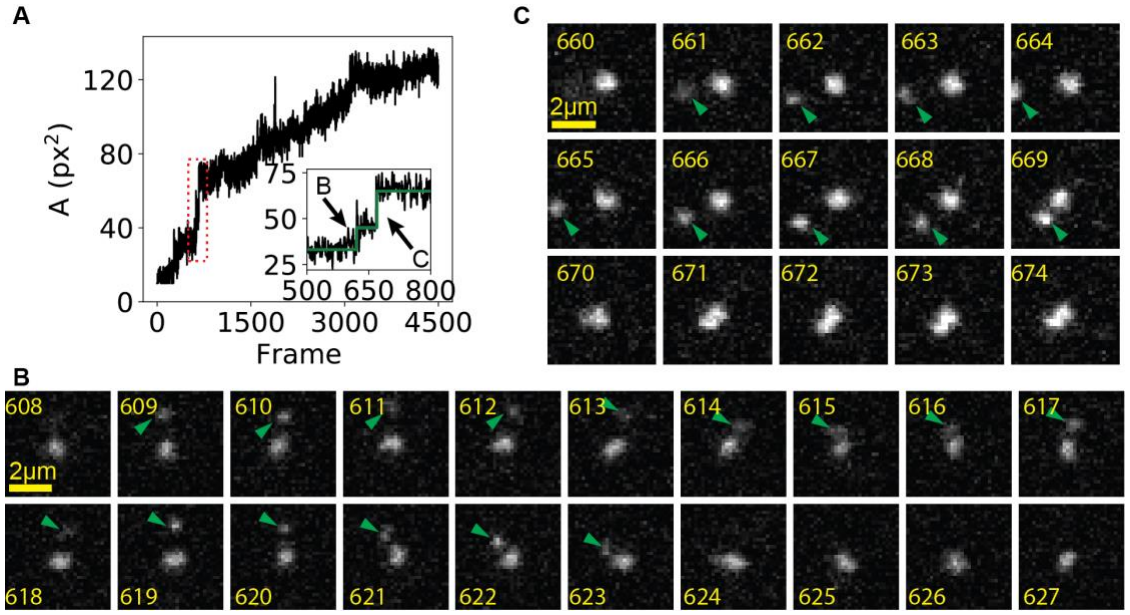

Figure 5. Addition of "monomers" to an AgNP-assembly. (**A**) The size of the assembly as a function of frame number (1 px = 160 nm, or 1 $px^2 = 2.56 \times 10^4$ nm^2). Inset: zoom-in of the region boxed by the red dashed rectangle. (**B**, **C**) Frame-by-frame montage of the movie for (B) frames 608–627 and (C) frames 660–674. Scale bars = 2 μm.

It was possible in our experiments to directly visualize the dynamic addition of a "monomer" to an assembly, especially for small assemblies or during the early assembling stage. As an example, the dynamic growth of a small assembly was shown in SI Movie M2, where the small assembly started as a dim, single AgNP. Quantifying the size of the assembly indicated that it grew steadily (Fig. 5A). More importantly, we observed distinct stepwise jumps in the early stage of the process. A close-up look of the red rectangular region of the curve was shown in the inset of Fig. 5A, where two steps were identified. By examining the frame-by-frame montages of the movie corresponding to the two steps (Fig. 5B and 5C), we observed that "monomers" diffused to the assembly and were then nanowelded to the assembly, leading to the "growth" of the assembly.

The simple analytical model was successful in describing the experimentally measured nanowelding/assembling kinetics of AgNPs; the predictions of the dependence of the kinetics on the laser power and initial concentration of AgNPs were also largely verified by experiments. However, the exact relation of fitted growth rate k on the laser power P deviated from linearity, which is followed by the dependence of the laser-induced LSPR and the associated temperature enhancement (and melting) on the laser power/intensity [41–43]. This deviation, together with the

imperfect global fitting of the data (Fig. 4A), indicated that the simple analytical model did not cover the full story of the nanowelding kinetics and that other factors or processes must be taken into account. For example, larger assemblies (or higher-order structures) could be formed from merging two smaller assemblies, in addition to adding monomers sequentially. Such merging of assemblies is expected to result in faster growth (and thus higher k). As a matter of fact, such process of assembly-merging was observed from our experiments (SI Movie M3), providing evidence for (partially) explaining the observed nonlinear k-P relation.

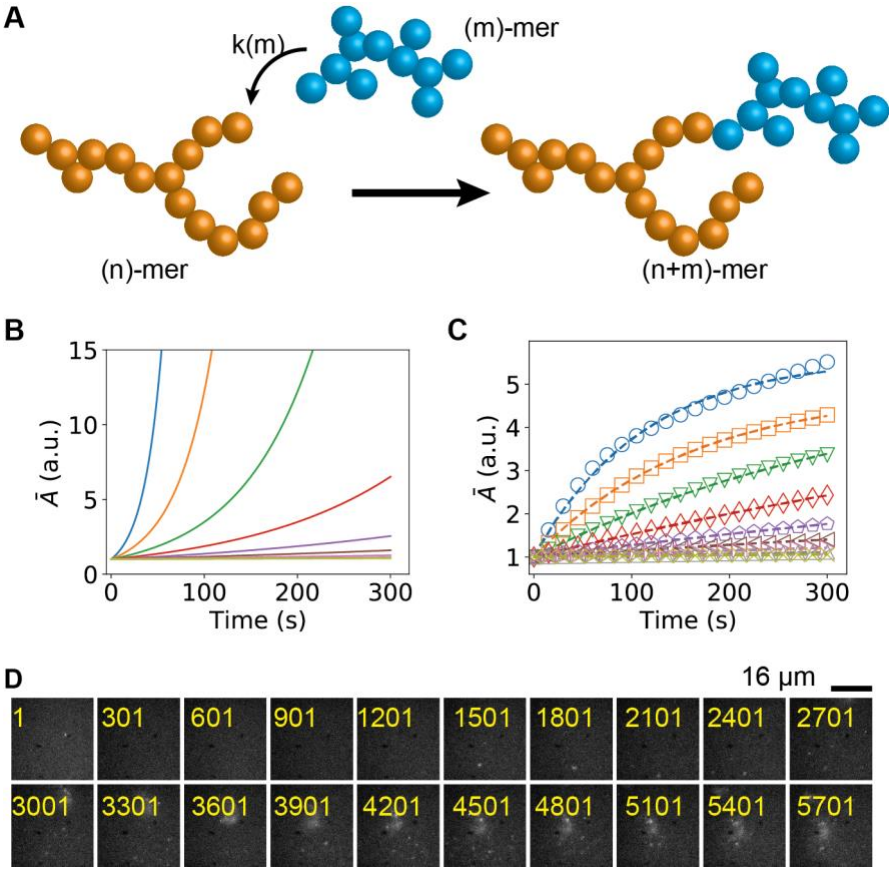

Figure 6. A generalized model that takes into account the merging of assemblies. (**A**) In the generalized model, two smaller assemblies with sizes of n and m, respectively, merge into a larger one of size $n + m$. (**B**) The predicted average sizes of the assemblies as functions of time from the generalized model with a constant merging rate $k(m) = k_1$ where k_1 is a constant. Colored solid lines correspond to different k_1. (**C**) The predicted average sizes of the assemblies as functions of time from the generalized model with size-dependent merging rates $k(m) = k_1/m$. Colored symbols correspond to different k_1. Colored dashed lines are fittings using $\bar{A}(t) = A_0 \times \left(1 - e^{-t/\tau}\right)$. (**D**) Slower nanowelding kinetics were observed for AgNPs in 50% glycerol illuminated by a 405 nm laser at a power level of 30% (~6 mW). Scale bar = 16 μm.

Numbers indicate the frame number of the acquired movie (frame rate = 19.05 fps).

To consider the merging process, we attempted to develop a more generalized model as sketched in Fig. 6A. Briefly, in this model, an assembly of size m can merge with an assembly of size n to form a larger assembly of size $n + m$ (Fig. 6A). Then, the revised differential equations became

$$\frac{dp_n}{dt} = \sum_{m=1}^{n-1} k\,(m) p_{n-m} p_m - \sum_{m=1}^{\infty} k\,(m) p_n p_m\,. \quad (7)$$

Numerically solving this set of equations, Eq. (7) and Eq. (4), would give the predicted kinetics from the generalized model. It is worthwhile to point out that the model asserted that the merging/assembling rate was dependent on the size of the smaller assemblies, $k = k(m)$. If the merging/assembling rate k is a constant, the model predicted exponentially increasing kinetics (Fig. 6B), which was inconsistent with our experimental observations (Fig. 2 and 4). The size-dependence of the rate (i.e., $k = k(m)$) implied that the nanowelding/assembling of AgNPs was significantly affected, or even limited, by the diffusion of the AgNPs. The implication was reasonable because of the elevation of the local temperature of the AgNPs (due to LSPR) [41–43] and thus the increase of their local diffusivity (e.g, $D = \frac{k_B T}{6\pi\eta r}$ for spheres with a radius of r in a solution with a viscosity of η, where T is the temperature and k_B is the Boltzmann constant). In addition, our observation of the addition of "monomers" to the assemblies suggested that diffusion played an important role in the nanowelding process (Fig. 5).

Although the solution for nanowelding kinetics from the generalized model depends on the exact size-dependence of the rate $k(m)$, we numerically solved the model for a simple case, $k(m) = k_1/m$ (where k_1 is a constant), which resembled the reciprocal relation in the Stokes-Einstein relation ($D \propto 1/r$). The rationale was that smaller assemblies of AgNPs diffuse faster, thus resulting in a higher merging/assembling rate. For this simple case, the model led to kinetic growth curves (Fig. 6C) that were consistent with the experimental measurements. The simulated kinetic curves could be also fitted well with Eq. (6) as shown in Fig. 6C.

Results from the generalized model indicated that the nanowelding kinetics was likely to be limited by the diffusion of the AgNPs. For experimental confirmation, we performed the same experiment with AgNPs in 50% glycerol illuminated by 405 nm at 30% power (~6 mW). The viscosity of 50% glycerol was much higher than that of water, leading to a lower diffusion coefficient of the AgNPs and thus a lower nanowelding/assembling rate. Our experiments showed that the laser-induced assemblies were formed at a much lower rate (Fig. 6D) in the 50%

glycerol, supporting the conclusion that the nanowelding kinetics was limited by the diffusion of the AgNPs.

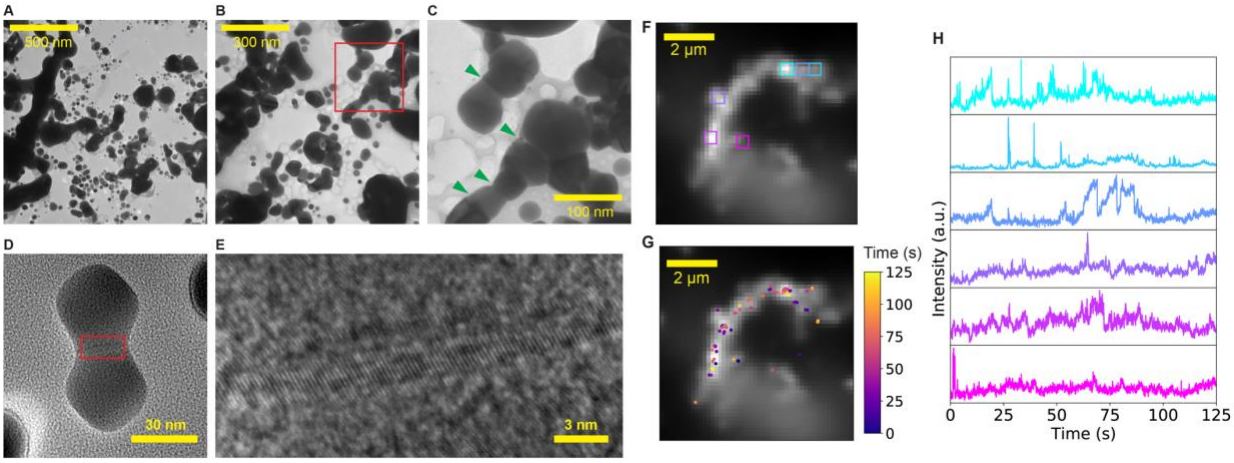

Figure 7. Separate photoluminescent domains in the laser-induced nanowelded assemblies of AgNPs. (**A**–**C**) Representative TEM images of the laser-induced assemblies of AgNPs with different zooming factors. Panel C is a close-up look of the region highlighted by the red square in panel B. Green arrows in panel C highlight the interfaces after nanowelding. (**D**) A representative HRTEM image of nanowelded AgNPs induced by the 405 nm laser. (**E**) A closer look of the nanowelding interface (i.e., the region highlighted by the red rectangle in panel D). (**F**) Examples of regions in the same assembly of AgNPs, showing different photoluminescence and blinking behaviors. (**G**) Photoluminescent intensities as functions of time for the regions highlighted in panel D with the corresponding colors. (**H**) Locations of flashing/blinking centers in the same assemblies of AgNPs. The color of the points indicates the time of the flashing/blinking.

It was reported previously that the laser-induced assemblies of nanoparticles formed single-phased ohmic nanocontact [11]. We performed TEM imaging on the assemblies of AgNPs and observed similar results (Fig. 7A–C). In addition, HRTEM imaging confirmed that the AgNPs were indeed fused/nanowelded (Fig. 7D), as indicated by the observed lattice fringes across the interface (Fig. 7E), instead of simply aggregated. However, we observed that the laser-induced assemblies were separated into domains of photoluminescence. For example, different regions of the same assembly (boxed regions in Fig. 7F) showed different photoluminescence intensities and blinking behaviors (SI Movie M4), which were seen clearly by comparing their intensity traces (Fig. 7G). The flashing/blinking at different regions was uncorrelated (Fig. 7G), suggesting that the laser-induced assemblies were not single-phased in terms of photoluminescent properties. In addition, we localized the centers of the flashing spots in the

single assembly [44–46] and observed that such flashing centers were distributed throughout the assembly (Fig. 7H). We speculated that the separation of photoluminescent domains was caused by grain boundaries at the nanoparticle attachment interfaces that were observed in the TEM images (Fig. 7C–E), and indirectly supported by the high-resolution TEM images in the literature [11]. It is expected that future experiments based on correlative photoluminescence and electron microscopy will provide direct, conclusive evidence for confirming / denying this speculation. Furthermore, previous studies reported that the quantum yield of the photoluminescence of AgNPs increased as the size decrease, while the larger nanowelded assemblies showed higher photoluminescence than the smaller individual AgNP in this study [47]; this discrepancy suggests the existence of separate photoluminescent domains in the nanowelded assemblies.

Conclusion and Discussion

In conclusion, we directly imaged the real-time laser-induced nanowelding/assembling kinetics of AgNPs using fluorescence microscopy. We observed that the AgNPs formed branched higher-order structures/assemblies upon illumination with a 405 nm CW laser. We quantified the sizes of the laser-induced assemblies, and more importantly, the assembling kinetics (i.e., as functions of time). We found that the dependence of the average size of the AgNP-assemblies on the illumination time followed $\bar{A} \propto 1 - e^{-t/\tau}$. To understand the measured kinetics, we developed a simple analytical model based on the polymerization argument. The analytical model predicted that $\bar{A} \propto c_0^2(1 - e^{-2kt})$, which was successful in describing the experimental results. In addition, we experimentally verified other predictions from the model, such as the dependence of the kinetics on the laser power and the initial concentration of the AgNPs. Furthermore, we improved the model by taking into account the merging of assemblies and predicted that the laser-induced assembling kinetics was diffusion-limited, which was then verified by experiments with AgNPs in 50% glycerol. Lastly, in contrast to the single-phased ohmic nanocontact produced by the laser-induced nanowelding, we found that the nanowelded assemblies of AgNPs were separated into photoluminescent domains: different regions in the same laser-induced assembly showed different photoluminescence and asynchronous uncorrelated blinking.

Previous studies reported that AgNPs with a size of 30 nm were photoluminescent [25,47,48]; the observation that the laser-induced assemblies of AgNPs showed higher photoluminescent intensities than single AgNPs when illuminated with a 405 nm laser (e.g., Fig. 2 and 5) facilitated photoluminescence imaging and allowed us to conveniently carry out the first direct, real-time imaging of the nanowelding/assembling kinetics of AgNPs. Other metallic nanoparticles (e.g., gold nanoparticles) have been reported to be photoluminescent [49–54];

therefore, we expect that the experimental method reported in this study will be useful for understanding the nanowelding kinetics of other metallic nanoparticles. In addition, it was shown previously that laser-induced LSPR of nanoparticles allowed for the creation of ohmic contacts among different metallic nanoparticles: one type of nanoparticles was surface-melted due to the LSPR and served as the liquid-like, soldering reagent, while the other type of nanoparticles was not melted, remaining solid-like under the laser illumination [55]. It would be interesting to directly visualize this "nanosoldering" process using multi-color fluorescence microscopy in the future.

In the current study, a laser of 405 nm was chosen for both LSPR excitation and photoluminescence imaging. It was chosen because 1) the wavelength is close to the LSPR peak of the AgNPs and 2) photoluminescent emission of AgNPs could be collected at this excitation due to the long tails in the emission spectrum (Fig. S6). We expect that other wavelengths may also be used. For example, the emission spectrum of the AgNPs showed similar, long photoluminescent tails when excited at 340 nm and 290 nm. We observed that the shape and intensity of the photoluminescence spectra of the same AgNPs were different for different excitations (Fig. S6), which was consistent with previous reports [47,48]. Although optimizing the excitation is out of the scope of the current study, it would be interesting to investigate in future studies how the laser wavelength affects the kinetics and other properties of the laser-induced nanowelding of metal nanoparticles.

We note that the "monomers" in our models for understanding the observed nanowelding/assembling kinetics do not necessarily correspond to single AgNPs, although individual AgNPs could possibly serve as monomers. However, it is worthwhile to point out that the measured exponential kinetics (i.e., $\propto 1 - e^{-t/\tau}$) were robust, not relying on the models nor what the "monomers" were. Nonetheless, it would be interesting to directly visualize the nanowelding of two single nanoparticles in real time. Recent development of *in situ* liquid cell electron microscopy [56–58] could be useful for this effort.

In contrast to femtosecond or picosecond pulsed lasers used in the literature for nanowelding nanoparticles [11,16,21,59], a CW laser at 405 nm was used in the current study. Considering that illumination of conventional fluorescent light was able to generate enough plasmon excitation and change the shape of nanoparticles [12,13], it is not surprising that CW lasers allowed nanowelding of nanoparticles, even if the peak power of CW lasers are typically much lower than pulsed ones. An advantage of exploiting a CW laser in the current study was that the lower peak power slowed down the melting of the surfaces of the nanoparticles, lowering the

requirement of temporal resolution in order to directly image the nanowelding kinetics in real-time.

Our results suggested that the laser-induced assemblies of AgNPs showed separate photoluminescent and blinking domains, unlike the single phase in the ohmic contact reported previously. We speculated that the separate photoluminescent domains were due to lattice mismatching, which generated interfaces in terms of photoluminescence. It is expected that high-resolution TEM will facilitate future studies in this direction.

This study showed that the nanowelding kinetics of AgNPs is dependent on external factors / conditions, such as laser power, concentration of nanoparticle, and viscosity of the environment. It would be interesting to further explore factors that influence the kinetics and properties of the nanowelding of nanoparticles, such as branching of the laser-induced assemblies and generation of LSPR hotspots. It is expected that this study and follow-up work will pave the way to better control and strategies of nanowelding processes to achieve desired structural features. For example, similar to generating different snowflakes by controlling temperature and water vapor supersaturation [60], it would be very interesting to produce, in a controlled way, different shapes of silver-flakes from AgNPs using laser-induced nanowelding, by modulating several parameters, such as laser wavelength, laser power, and composition of solution.

Acknowledgment

This work was supported by the National Science Foundation (grant no. CBET 1826642) and the Arkansas Biosciences Institute (grant no. ABI-0189, ABI-0226, ABI-0277, ABI-0326, and ABI-2021). We are also grateful for support from the Arkansas High Performance Computing Center (AHPCC), which is funded in part by the National Science Foundation (grant no. 0722625, 0959124, 0963249, and 0918970) and the Arkansas Science and Technology Authority.

References

(1) Govorov, A. O.; Richardson, H. H. Generating Heat with Metal Nanoparticles. *Nano Today* **2007**, *2* (1), 30–38. https://doi.org/10.1016/S1748-0132(07)70017-8.

(2) Li, H.; He, Y.; Wang, C.; Wang, X.; Hu, Y. Tunable Thermal and Electricity Generation Enabled by Spectrally Selective Absorption Nanoparticles for Photovoltaic/Thermal Applications. *Applied Energy* **2019**, *236*, 117–126. https://doi.org/10.1016/j.apenergy.2018.11.085.

(3) Naito, M.; Yokoyama, T.; Hosokawa, K.; Nogi, K. *Nanoparticle Technology Handbook*; Elsevier, 2018.
(4) Praetorius, A.; Scheringer, M.; Hungerbühler, K. Development of Environmental Fate Models for Engineered Nanoparticles—A Case Study of TiO2 Nanoparticles in the Rhine River. *Environ. Sci. Technol.* **2012**, *46* (12), 6705–6713. https://doi.org/10.1021/es204530n.
(5) Sarina, S.; Waclawik, E. R.; Zhu, H. Photocatalysis on Supported Gold and Silver Nanoparticles under Ultraviolet and Visible Light Irradiation. *Green Chem.* **2013**, *15* (7), 1814–1833. https://doi.org/10.1039/C3GC40450A.
(6) Xin, S.; Shen, J.; Liu, G.; Chen, Q.; Xiao, Z.; Zhang, G.; Xin, Y. Electricity Generation and Microbial Community of Single-Chamber Microbial Fuel Cells in Response to Cu2O Nanoparticles/Reduced Graphene Oxide as Cathode Catalyst. *Chemical Engineering Journal* **2020**, *380*, 122446. https://doi.org/10.1016/j.cej.2019.122446.
(7) Yin, Y.; Rioux, R. M.; Erdonmez, C. K.; Hughes, S.; Somorjai, G. A.; Alivisatos, A. P. Formation of Hollow Nanocrystals Through the Nanoscale Kirkendall Effect. *Science* **2004**, *304* (5671), 711–714. https://doi.org/10.1126/science.1096566.
(8) Cha, S.-H.; Park, Y.; Han, J. W.; Kim, K.; Kim, H.-S.; Jang, H.-L.; Cho, S. Cold Welding of Gold Nanoparticles on Mica Substrate: Self-Adjustment and Enhanced Diffusion. *Scientific Reports* **2016**, *6* (1), 32951. https://doi.org/10.1038/srep32951.
(9) Kong, X. Y.; Ding, Y.; Yang, R.; Wang, Z. L. Single-Crystal Nanorings Formed by Epitaxial Self-Coiling of Polar Nanobelts. *Science* **2004**, *303* (5662), 1348–1351. https://doi.org/10.1126/science.1092356.
(10) Yan, F.; Goedel, W. A. Preparation of Mesoscopic Gold Rings Using Particle Imprinted Templates. *Nano Lett.* **2004**, *4* (7), 1193–1196. https://doi.org/10.1021/nl0497169.
(11) Kim, S. J.; Jang, D.-J. Laser-Induced Nanowelding of Gold Nanoparticles. *Appl. Phys. Lett.* **2005**, *86* (3), 033112. https://doi.org/10.1063/1.1856139.
(12) Jin, R.; Cao, Y.; Mirkin, C. A.; Kelly, K. L.; Schatz, G. C.; Zheng, J. G. Photoinduced Conversion of Silver Nanospheres to Nanoprisms. *Science* **2001**, *294* (5548), 1901–1903. https://doi.org/10.1126/science.1066541.
(13) Jin, R.; Charles Cao, Y.; Hao, E.; Métraux, G. S.; Schatz, G. C.; Mirkin, C. A. Controlling Anisotropic Nanoparticle Growth through Plasmon Excitation. *Nature* **2003**, *425* (6957), 487–490. https://doi.org/10.1038/nature02020.
(14) Catone, D.; Ciavardini, A.; Di Mario, L.; Paladini, A.; Toschi, F.; Cartoni, A.; Fratoddi, I.; Venditti, I.; Alabastri, A.; Proietti Zaccaria, R.; O'Keeffe, P. Plasmon Controlled Shaping of Metal Nanoparticle Aggregates by Femtosecond Laser-Induced Melting. *J. Phys. Chem. Lett.* **2018**, *9* (17), 5002–5008. https://doi.org/10.1021/acs.jpclett.8b02117.
(15) Zhao, Z.-J.; Shin, S.-H.; Choi, D.-G.; Park, S.-H.; Jeong, J.-H. Shape-Controlled 3D Periodic Metal Nanostructures Fabricated via Nanowelding. *Small* **2018**, *14* (6), 1703102. https://doi.org/10.1002/smll.201703102.
(16) Herrmann, L. O.; Valev, V. K.; Tserkezis, C.; Barnard, J. S.; Kasera, S.; Scherman, O. A.; Aizpurua, J.; Baumberg, J. J. Threading Plasmonic Nanoparticle Strings with Light. *Nature Communications* **2014**, *5* (1), 4568. https://doi.org/10.1038/ncomms5568.
(17) Zhang, D.; Gökce, B.; Barcikowski, S. Laser Synthesis and Processing of Colloids: Fundamentals and Applications. *Chem Rev* **2017**, *117* (5), 3990–4103. https://doi.org/10.1021/acs.chemrev.6b00468.

(18) Marchuk, K.; Willets, K. A. Localized Surface Plasmons and Hot Electrons. *Chem Phys* **2014**, *445*, 95–104. https://doi.org/10.1016/j.chemphys.2014.10.016.
(19) Petryayeva, E.; Krull, U. J. Localized Surface Plasmon Resonance: Nanostructures, Bioassays and Biosensing—A Review. *Analytica Chimica Acta* **2011**, *706* (1), 8–24. https://doi.org/10.1016/j.aca.2011.08.020.
(20) González-Rubio, G.; Guerrero-Martínez, A.; Liz-Marzán, L. M. Reshaping, Fragmentation, and Assembly of Gold Nanoparticles Assisted by Pulse Lasers. *Acc. Chem. Res.* **2016**, *49* (4), 678–686. https://doi.org/10.1021/acs.accounts.6b00041.
(21) Garnett, E. C.; Cai, W.; Cha, J. J.; Mahmood, F.; Connor, S. T.; Greyson Christoforo, M.; Cui, Y.; McGehee, M. D.; Brongersma, M. L. Self-Limited Plasmonic Welding of Silver Nanowire Junctions. *Nature Materials* **2012**, *11* (3), 241–249. https://doi.org/10.1038/nmat3238.
(22) González-Rubio, G.; Díaz-Núñez, P.; Rivera, A.; Prada, A.; Tardajos, G.; González-Izquierdo, J.; Bañares, L.; Llombart, P.; Macdowell, L. G.; Alcolea Palafox, M.; Liz-Marzán, L. M.; Peña-Rodríguez, O.; Guerrero-Martínez, A. Femtosecond Laser Reshaping Yields Gold Nanorods with Ultranarrow Surface Plasmon Resonances. *Science* **2017**, *358* (6363), 640–644. https://doi.org/10.1126/science.aan8478.
(23) Zhang, Q.; Li, W.; Moran, C.; Zeng, J.; Chen, J.; Wen, L.-P.; Xia, Y. Seed-Mediated Synthesis of Ag Nanocubes with Controllable Edge Lengths in the Range of 30-200 Nm and Comparison of Their Optical Properties. *J Am Chem Soc* **2010**, *132* (32), 11372–11378. https://doi.org/10.1021/ja104931h.
(24) Haque, M. A.; Imamura, R.; Brown, G. A.; Krishnamurthi, V. R.; Niyonshuti, I. I.; Marcelle, T.; Mathurin, L. E.; Chen, J.; Wang, Y. An Experiment-Based Model Quantifying Antimicrobial Activity of Silver Nanoparticles OnEscherichia Coli. *RSC Adv.* **2017**, *7* (89), 56173–56182. https://doi.org/10.1039/C7RA10495B.
(25) Alqahtany, M.; Khadka, P.; Niyonshuti, I.; Krishnamurthi, V. R.; Sadoon, A. A.; Challapalli, S. D.; Chen, J.; Wang, Y. Nanoscale Reorganizations of Histone-like Nucleoid Structuring Proteins in Escherichia Coli Are Caused by Silver Nanoparticles. *Nanotechnology* **2019**, *30* (38), 385101. https://doi.org/10.1088/1361-6528/ab2a9f.
(26) Niyonshuti, I. I.; Krishnamurthi, V. R.; Okyere, D.; Song, L.; Benamara, M.; Tong, X.; Wang, Y.; Chen, J. Polydopamine Surface Coating Synergizes the Antimicrobial Activity of Silver Nanoparticles. *ACS Appl. Mater. Interfaces* **2020**, *12* (36), 40067–40077. https://doi.org/10.1021/acsami.0c10517.
(27) Laramy, C. R.; Brown, K. A.; O'Brien, M. N.; Mirkin, Chad. A. High-Throughput, Algorithmic Determination of Nanoparticle Structure from Electron Microscopy Images. *ACS Nano* **2015**, *9* (12), 12488–12495. https://doi.org/10.1021/acsnano.5b05968.
(28) Draine, B. T.; Flatau, P. J. Discrete-Dipole Approximation for Periodic Targets: Theory and Tests. *J. Opt. Soc. Am. A, JOSAA* **2008**, *25* (11), 2693–2703. https://doi.org/10.1364/JOSAA.25.002693.
(29) Draine, B. T.; Flatau, P. J. User Guide for the Discrete Dipole Approximation Code DDSCAT 7.3. **2013**.
(30) Johnson, P. B.; Christy, R. W. Optical Constants of the Noble Metals. *Phys. Rev. B* **1972**, *6* (12), 4370–4379. https://doi.org/10.1103/PhysRevB.6.4370.
(31) Wang, Y.; Cai, E.; Sheung, J.; Lee, S. H.; Teng, K. W.; Selvin, P. R. Fluorescence Imaging with One-Nanometer Accuracy (FIONA). *J Vis Exp* **2014**, No. 91, 51774. https://doi.org/10.3791/51774.

(32) Selvin, P. R.; Ha, T. *Single Molecule Techniques: A Laboratory Manual*, 1st ed.; Cold Spring Harbor Laboratory Press: Cold Spring Harbor, N.Y, 2007.
(33) Edelstein, A.; Amodaj, N.; Hoover, K.; Vale, R.; Stuurman, N. Computer Control of Microscopes Using MManager. *Curr Protoc Mol Biol* **2010**, *Chapter 14*, Unit14.20. https://doi.org/10.1002/0471142727.mb1420s92.
(34) Edelstein, A. D.; Tsuchida, M. A.; Amodaj, N.; Pinkard, H.; Vale, R. D.; Stuurman, N. Advanced Methods of Microscope Control Using MManager Software. *J Biol Methods* **2014**, *1* (2). https://doi.org/10.14440/jbm.2014.36.
(35) van der Walt, S.; Schönberger, J. L.; Nunez-Iglesias, J.; Boulogne, F.; Warner, J. D.; Yager, N.; Gouillart, E.; Yu, T.; scikit-image contributors. Scikit-Image: Image Processing in Python. *PeerJ* **2014**, *2*, e453. https://doi.org/10.7717/peerj.453.
(36) Sternberg. Biomedical Image Processing. *Computer* **1983**, *16* (1), 22–34. https://doi.org/10.1109/MC.1983.1654163.
(37) Kanopoulos, N.; Vasanthavada, N.; Baker, R. L. Design of an Image Edge Detection Filter Using the Sobel Operator. *IEEE Journal of Solid-State Circuits* **1988**, *23* (2), 358–367. https://doi.org/10.1109/4.996.
(38) Nosal, E. Flood-Fill Algorithms Used for Passive Acoustic Detection and Tracking. In *2008 New Trends for Environmental Monitoring Using Passive Systems*; 2008; pp 1–5. https://doi.org/10.1109/PASSIVE.2008.4786975.
(39) Phillips, R.; Kondev, J.; Theriot, J.; Garcia, H. *Physical Biology of the Cell*; Garland Science, 2012.
(40) Newville, M.; Stensitzki, T.; Allen, D. B.; Ingargiola, A. *LMFIT: Non-Linear Least-Square Minimization and Curve-Fitting for Python*; Zenodo, 2014. https://doi.org/10.5281/zenodo.11813.
(41) Jiang, K.; Smith, D. A.; Pinchuk, A. Size-Dependent Photothermal Conversion Efficiencies of Plasmonically Heated Gold Nanoparticles. *J. Phys. Chem. C* **2013**, *117* (51), 27073–27080. https://doi.org/10.1021/jp409067h.
(42) Richardson, H. H.; Carlson, M. T.; Tandler, P. J.; Hernandez, P.; Govorov, A. O. Experimental and Theoretical Studies of Light-to-Heat Conversion and Collective Heating Effects in Metal Nanoparticle Solutions. *Nano Lett* **2009**, *9* (3), 1139–1146. https://doi.org/10.1021/nl8036905.
(43) Baffou, G.; Quidant, R.; García de Abajo, F. J. Nanoscale Control of Optical Heating in Complex Plasmonic Systems. *ACS Nano* **2010**, *4* (2), 709–716. https://doi.org/10.1021/nn901144d.
(44) Wang, Y.; Fruhwirth, G.; Cai, E.; Ng, T.; Selvin, P. R. 3D Super-Resolution Imaging with Blinking Quantum Dots. *Nano Lett* **2013**, *13* (11), 5233–5241. https://doi.org/10.1021/nl4026665.
(45) Simonson, P. D.; Rothenberg, E.; Selvin, P. R. Single-Molecule-Based Super-Resolution Images in the Presence of Multiple Fluorophores. *Nano Lett.* **2011**, *11* (11), 5090–5096. https://doi.org/10.1021/nl203560r.
(46) Burnette, D. T.; Sengupta, P.; Dai, Y.; Lippincott-Schwartz, J.; Kachar, B. Bleaching/Blinking Assisted Localization Microscopy for Superresolution Imaging Using Standard Fluorescent Molecules. *PNAS* **2011**, *108* (52), 21081–21086. https://doi.org/10.1073/pnas.1117430109.
(47) Yeshchenko, O. A.; Dmitruk, I. M.; Alexeenko, A. A.; Losytskyy, M. Yu.; Kotko, A. V.; Pinchuk, A. O. Size-Dependent Surface-Plasmon-Enhanced Photoluminescence from

Silver Nanoparticles Embedded in Silica. *Phys. Rev. B* **2009**, *79* (23), 235438. https://doi.org/10.1103/PhysRevB.79.235438.
(48) Zhang, A.; Zhang, J.; Fang, Y. Photoluminescence from Colloidal Silver Nanoparticles. *Journal of Luminescence* **2008**, *128* (10), 1635–1640. https://doi.org/10.1016/j.jlumin.2008.03.014.
(49) He, H.; Xie, C.; Ren, J. Nonbleaching Fluorescence of Gold Nanoparticles and Its Applications in Cancer Cell Imaging. *Anal. Chem.* **2008**, *80* (15), 5951–5957. https://doi.org/10.1021/ac8005796.
(50) Geddes, C. D.; Parfenov, A.; Gryczynski, I.; Lakowicz, J. R. Luminescent Blinking of Gold Nanoparticles. *Chemical Physics Letters* **2003**, *380* (3), 269–272. https://doi.org/10.1016/j.cplett.2003.07.029.
(51) Geddes, C. D.; Parfenov, A.; Lakowicz, J. R. Luminescent Blinking from Noble-Metal Nanostructures: New Probes for Localization and Imaging. *Journal of Fluorescence* **2003**, *13* (4), 297–299. https://doi.org/10.1023/A:1025369509842.
(52) Gaiduk, A.; Ruijgrok, P. V.; Yorulmaz, M.; Orrit, M. Making Gold Nanoparticles Fluorescent for Simultaneous Absorption and Fluorescence Detection on the Single Particle Level. *Phys. Chem. Chem. Phys.* **2010**, *13* (1), 149–153. https://doi.org/10.1039/C0CP01389G.
(53) Wolfbeis, O. S. An Overview of Nanoparticles Commonly Used in Fluorescent Bioimaging. *Chem. Soc. Rev.* **2015**, *44* (14), 4743–4768. https://doi.org/10.1039/C4CS00392F.
(54) Qing, Z.; He, X.; Qing, T.; Wang, K.; Shi, H.; He, D.; Zou, Z.; Yan, L.; Xu, F.; Ye, X.; Mao, Z. Poly(Thymine)-Templated Fluorescent Copper Nanoparticles for Ultrasensitive Label-Free Nuclease Assay and Its Inhibitors Screening. *Anal. Chem.* **2013**, *85* (24), 12138–12143. https://doi.org/10.1021/ac403354c.
(55) Mafuné, F.; Kohno, J.-Y.; Takeda, Y.; Kondow, T. Nanoscale Soldering of Metal Nanoparticles for Construction of Higher-Order Structures. *J Am Chem Soc* **2003**, *125* (7), 1686–1687. https://doi.org/10.1021/ja021250d.
(56) Williamson, M. J.; Tromp, R. M.; Vereecken, P. M.; Hull, R.; Ross, F. M. Dynamic Microscopy of Nanoscale Cluster Growth at the Solid–Liquid Interface. *Nature Materials* **2003**, *2* (8), 532–536. https://doi.org/10.1038/nmat944.
(57) de Jonge, N.; Ross, F. M. Electron Microscopy of Specimens in Liquid. *Nature Nanotechnology* **2011**, *6* (11), 695–704. https://doi.org/10.1038/nnano.2011.161.
(58) Chen, L.; Leonardi, A.; Chen, J.; Cao, M.; Li, N.; Su, D.; Zhang, Q.; Engel, M.; Ye, X. Imaging the Kinetics of Anisotropic Dissolution of Bimetallic Core–Shell Nanocubes Using Graphene Liquid Cells. *Nature Communications* **2020**, *11* (1), 3041. https://doi.org/10.1038/s41467-020-16645-3.
(59) Hu, A.; Zhou, Y.; W. Duley, W. Femtosecond Laser-Induced Nanowelding: Fundamentals and Applications. *The Open Surface Science Journal* **2011**, *3* (1).
(60) Libbrecht, K. G. Physical Dynamics of Ice Crystal Growth. *Annual Review of Materials Research* **2017**, *47* (1), 271–295. https://doi.org/10.1146/annurev-matsci-070616-124135.